Journal of Low Temperature Physics (2023) 212:138–152
https://doi.org/10.1007/s10909-023-02979-x

Development of Low-Threshold Detectors for Low-Mass Dark Matter Searches with a p-Type Germanium Detector Operated at Cryogenic Temperature

Mathbar Singh Raut[1] · Dongming Mei[1] · Sanjay Bhattarai[1] · Rajendra Panth[1] · Kyler Kooi[1] · Hao Mei[1] · Guojian Wang[1]

Received: 29 March 2023 / Accepted: 13 May 2023 / Published online: 20 June 2023

Abstract
This study investigates new technology for enhancing the sensitivity of low-mass dark matter detection by analyzing charge transport in a p-type germanium detector at 5.2 K. To achieve low-threshold detectors, precise calculations of the binding energies of dipole and cluster dipole states, as well as the cross sections of trapping affected by the electric field, are essential. The detector was operated in two modes: depleted at 77 K before cooling to 5.2 K and cooled directly to 5.2 K with various bias voltages. Our results indicate that the second mode produces lower binding energies and suggests different charge states under varying operating modes. Notably, our measurements of the dipole and cluster dipole state binding energies at zero fields were 8.716 ± 0.435 meV and 6.138 ± 0.308 meV, respectively. These findings have strong implications for the development of low-threshold detectors for detecting low-mass dark matter in the future.

Keywords Dipole states · Cluster dipole states · Binding energy · Dark matter · Low-threshold detectors

1 Introduction

The interaction between dark matter (DM) and ordinary matter results in only a small amount of energy being deposited through nuclear or electron recoil, which is limited to weak elastic scattering processes [1, 2]. Therefore, detectors with extremely low energy thresholds are required to detect DM [3–5]. Despite the modest mass of MeV-scale DM, its recent recognition as a potential DM candidate has generated interest. Unfortunately, current large-scale experiments are unable to

✉ Dongming Mei
dongming.mei@usd.edu

[1] University of South Dakota, Vermillion 57069, SD, USA

detect MeV-scale DM due to its low mass. To detect MeV-scale DM, new detectors with sub-eV thresholds are needed as both electronic and nuclear recoils from MeV-scale DM range from sub-eV to 100 eV [6–8].

The detection of low-mass DM using conventional techniques is challenging. However, germanium (Ge) detectors offer a promising solution as they have the lowest energy threshold among current detector technologies, making them ideal for low-mass DM searches [2, 9–11]. Ge has a bandgap of 0.7 eV at 77 K, and an average energy of 3 eV is required to generate an electron–hole pair [12]. This lower bandgap in Ge is very favorable for the detection of low-mass DM. Furthermore, proper doping of the Ge detector with impurities can expand the parameter space for low-mass DM searches. Shallow-level impurities in Ge detectors have binding energies of about 0.01 eV, which can form dipole states and cluster dipole states at temperatures below 10 K [13, 14]. These states have even lower binding energies than the impurities themselves, offering a potential avenue for detecting low-mass DM. Although the binding energies of impurities in Ge are well understood [15, 16], the binding energies of the dipole states and cluster dipole states near helium temperature is still poorly understood.

As temperatures approach liquid helium levels, any remaining impurities in Ge detectors freeze out of the conduction or valence band and transit into localized states, forming electric dipoles (D^{0*} for donors and A^{0*} for acceptors) or neutral states (D^0 and A^0) [13]. These dipole states have the ability to trap charge carriers and can form cluster dipole states (D^+ and D^- for donors, and A^+ and A^- for acceptors) [13]. Figure 1 depicts the formation of dipole states and cluster dipole states at temperatures below 10 K.

Previous studies by Mei et al. have thoroughly examined this phenomenon [13]. When an alpha particle (α) from ^{241}Am decay is directed toward a Ge detector, it creates electron–hole pairs within a range of 10 μm from the detector's surface [17–19]. By operating the detector at a cryogenic temperature of approximately 4 K

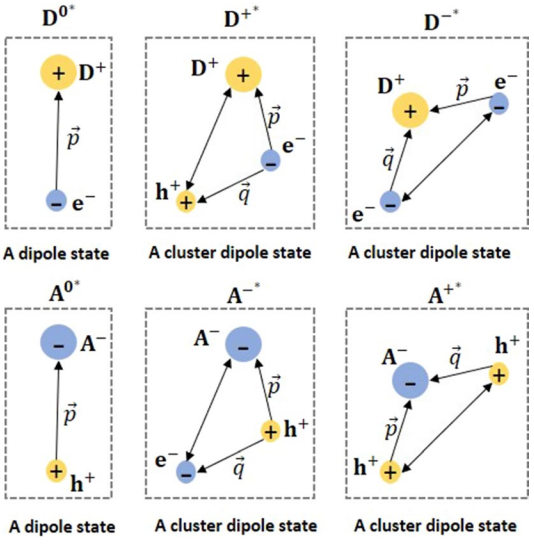

Fig. 1 An illustration of the processes that lead to the development of excited dipole states and cluster dipole states in an n-type (upper) and a p-type (lower) Ge detector operated at temperatures below 10 K, where $\vec{p}$ and $\vec{q}$ are the corresponding dipole moments [13]

and applying a positive or negative bias voltage to the bottom of the detector, only one type of charge carriers is drifted through it. To study the binding energy of the formed dipole states and cluster dipole states, these drifted charge carriers undergo a dynamic process of elastic scattering, trapping, and de-trapping. In this experiment, a p-type Ge detector is run in two different modes with different bias voltages while being cooled to cryogenic temperature. Similar experiment and its results for an n-type Ge detector operating in these two modes have already been published [20].

2 Experimental Procedure

The state-of-the-art infrastructure at USD for crystal growth and detector development includes a zone refining process for highly purifying commercial ingots, which can be used for crystal growth with the Czochralski method [21–24]. This enables the USD detector fabrication laboratory to produce superior homegrown crystals that are utilized for creating p-type (RL) detector with a net impurity concentration of $6.2 \times 10^9/\text{cm}^3$ and dimensions of 18.8 mm × 17.9 mm × 10.7 mm. The detector was fabricated using a sputtering technique, which deposits an amorphous Ge layer on the top, sides, and bottom of the detector to form electrical contacts. The detailed fabrication process has been published in our previous work titled "Fabrication and Characterization of High-Purity Germanium Detectors with Amorphous Germanium Contacts" by Meng et al. [25]. To ensure optimum electrical performance, an amorphous Ge passivation layer of 600 nm is applied to the surface of the Ge crystal as the electrical interface to successfully block surface charges [12, 26].

The detector is mounted inside a pulse tube refrigerator, which cools it down to nearly liquid helium temperature from room temperature. To ensure accurate temperature measurements, we have installed two temperature sensors inside the detector housing. One sensor is placed at the bottom of a copper plate on which the detector rests on a thin indium foil, while the other is located on top of another copper plate close to the top surface of the detector. By positioning the detector between these two sensors, we can measure its temperature with an accuracy of 0.5 K. The temperature readings from the two sensors are always within 0.5 K of each other.

We chose a working temperature of 5.2 K based on the capacitance measurements presented in Ref. [13]. The capacitance measurements indicate that the capacitance remains constant when the temperature is below 6.5 K. To ensure that the capacitance remains stable and to err on the side of caution, we chose a working temperature of 5.2 K.

In the experiment, an alpha source (^{241}Am) was placed near the detector inside a cryostat to measure the energy deposition of α-particles, creating localized electron–hole pairs near the top surface of the detector. By applying a negative bias voltage to the bottom of the detector, the holes are drifted through the detector. The experiment was conducted using two modes of operation.

In Mode 1, the RL detector was operated at 77 K with a depletion voltage of − 400 V and an operational voltage of − 1200 V. An α-source (^{241}Am) emitting α-particles with energy of ∼ 5.5 MeV was placed in close proximity to the detector inside the cryostat. The resulting energy spectrum was measured to detect the energy deposition of the ∼ 5.5 MeV α-particles, which was visible as a 3.92 MeV energy peak due to energy

loss en route to the detector's active region. The negligible detector charge trapping at 77 K with a bias of − 1200 V made the 3.92 MeV energy deposition an ideal reference for determining the energy deposition of ∼ 5.5 MeV alpha particles in the p-type detector without charge trapping. To calculate the charge collection efficiency, the measured alpha energy peak was divided by 3.92 MeV for a specific bias voltage.

The detector was cooled down to 5.2 K and maintained fully depleted by a negative bias voltage of − 1200 V. Following α energy deposition on the detector's surface, the resulting holes began to drift across the detector. At this temperature, space charge could trap holes, leading to the formation of electric dipole states. To investigate these states, the detector was subjected to decreasing bias voltages ranging from − 1200 to − 200 V. Energy deposition histograms of alpha particles were recorded every 2–3 min for a duration of 60 min at each bias voltage, enabling the collection of data on the dipole states and their properties.

When operating in Mode 2, the detector was grounded during the cool-down process and the detector was cooled immediately to 5.2 K without any bias voltage applied. Once the temperature reached 5.2 K, a negative bias voltage was gradually applied from the bottom of the detector, creating an electric field that caused the surface-generated holes to drift across the detector. The energy spectrum measurements were taken using bias voltages of − 200, − 300, − 600, − 900, and − 1100 V. As in Mode 1, data were collected for 60 min at each bias voltage, with histograms of energy deposition by alpha particles recorded every 2–3 min.

Figures 2 and 3 illustrate the energy deposition of the 5.5 MeV α particles emitted from ^{241}Am decays when the detector was operated in Mode 1 and Mode 2,

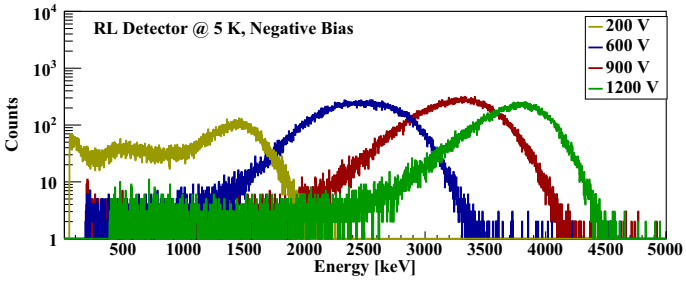

Fig. 2 The energy deposition of ∼ 5.5 MeV α particles in an p-type detector operating in Mode 1

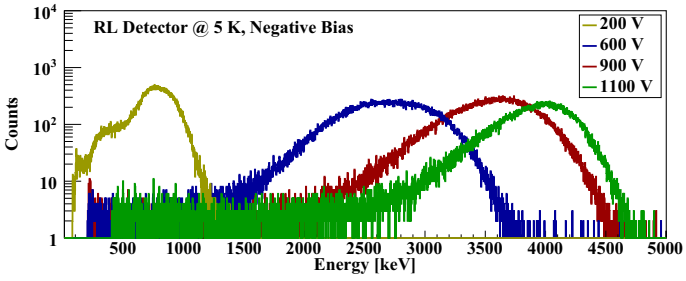

Fig. 3 The energy deposition of ∼ 5.5 MeV α particles in an p-type detector operating in Mode 2

respectively. Both modes were designed to investigate different physical processes, which are explained below in terms of their physical processes.

2.1 Mode 1

A p-type planar detector is first cooled to 77 K in this mode, and then a negative bias voltage is applied to the bottom of the detector, gradually raising it until the detector is completely depleted at − 400 V. After that the bias is elevated by an additional 800 volts to reach the operational voltage. The detector is then brought under the operational voltage while being cooled down to 5.2 K. At 77 K, the depletion process causes all the free-charge carriers to be swept away, leaving only the space charge states, A^{-}, behind. Upon cooling to 5.2 K, a trapping process occurs. As the holes continue to drift across the detector, the de-trapping process occurs [13]. The key trapping and de-trapping processes are described below:

$$h^{+} + A^{-} \rightarrow A^{0*}; h^{+} + A^{0*} \rightarrow A^{-} + 2h^{+}. \tag{1}$$

When the detector is operated in negative bias at the bottom, the Coulomb force between the space charge states and the drifting holes occurs. The p-type planar detector's operation in this mode starts with the formation of dipole states through charge trapping. Charge de-trapping, also known as the second process, involves releasing trapped charge by ionizing the dipole states through impact ionization.

We can figure out the binding energy of the dipole states by looking at the time-dependent behavior of this de-trapping process.

2.2 Mode 2

The p-type planar Ge detector is directly cooled to 5.2 K in this mode of operation, with no bias voltage provided. The detector is then biased to the required voltage level after cooling. Impurities in the Ge crystal freeze out of the conduction or valence band at very low temperatures, forming localized states that give rise to dipole states. As it is a p-type detector, the majority of these dipole states are A^{0*} [13]. When an α source is positioned near the detector, electron–hole pairs are created on the detector's surface. The resulting holes then drift across the detector upon application of a negative bias voltage to its bottom. This initiates the following processes within the detector:

$$h^{+} + A^{0^{*}} \rightarrow A^{+^{*}}; h^{+} + A^{+^{*}} \rightarrow 2h^{+} + A^{0^{*}}. \tag{2}$$

Operation of the detector in a negative bias mode leads to the production of cluster dipole states as the initial process. These states arise from the Coulomb forces exerted on the drifting holes, resulting in the trapping of charges. The second process involves the impact ionization of the cluster dipole states, leading to the

de-trapping of charges. Charge production, generation, and transport occur dynamically within the detector, and the study of the time-dependent de-trapping of charges through the impact ionization of cluster dipole states can provide insights into their binding energies.

It is important to note that when comparing the two operational modes, Mode 2 creates the dipole states at 5.2 K without the requirement for a bias voltage to be applied. When the holes cross the detector, these dipole states quickly trap the charges, resulting in a shorter trapping time and lower binding energy. In contrast, when an applied bias voltage causes holes to drift across the detector, Mode 1 produces the dipole states in the space charge area. The trapping time is therefore anticipated to be longer and the binding energy of the dipole states to be larger than that of the cluster dipoles.

3 Physical Model

The following concepts highlight the physics model employed in this investigation. A cryogenically cooled HPGe detector placed near an α source causes free charge carriers to drift along the detector and become captured in electric dipole states, forming cluster dipole states. The increase in cluster dipole states is accompanied by a decrease in electric dipole states, indicating a reduction in charge trapping. Charge carriers trapped in the cluster dipole states begin to emit from the traps upon continuously biasing the detector. The emission rate of these charge carriers is time-dependent and reaches saturation once all of the trapped carriers have been released. The emission rate can be determined using references such as [27, 28]:

$$e_n = \sigma_{\text{trap}} v_{\text{th}} N_v \exp\left(\frac{-E_B}{k_B T}\right), \tag{3}$$

where σ_{trap} is the trapping cross section, v_{th} is the thermal velocity, N_v is the effective density of states of holes in the valence band, E_B is the binding energy of the trapped charge carriers, k_B is the Boltzmann constant, and T is the temperature of the detector.

Equation 3 can be used to obtain the binding energy of dipole states or cluster dipole states if the trapping cross section (σ_{trap}) is known, provided that experimental data is used to determine e_n directly, along with the values of v_{th}, N_v, and T. However, determining the value of σ_{trap} requires additional calculations, as will be explained below.

The relationship between the trapping cross section of charge carriers and the trapping length λ_{trap} is described by the following equation [29, 30]:

$$\lambda_{\text{trap}} = \frac{1}{\left(\frac{N_A+N_D \pm |N_A-N_D|}{2}\right) \times \left(\sigma_{\text{trap}} \times \frac{v_{\text{tot}}}{v_d}\right)}, \tag{4}$$

Where N_A and N_D represent the p-type and n-type impurities, respectively. Note that the method we used to determine these densities is consistent with that used in our

previous publication [29]. Our findings indicate that there is a factor of approximately 10 difference between N_A and N_D, which allows us to utilize N_A–N_D as a suitable representation of N_A. v_{tot} is the total velocity of the drift holes, and v_d is the drift velocity, which is electric field dependent and is given by [14],

$$v_d \approx \frac{\mu_0 E}{\left(1 + \frac{\mu_0 E}{v_{\text{sat}}}\right)}, \tag{5}$$

where μ_0 is the mobility of the charge carrier when the field is zero and is equal to

$$\mu_0 = \frac{\mu_0(H)}{r}, \tag{6}$$

and $\mu_0(H)$ is the Hall mobility. The IEEE standard values for $\mu_0(H)$ and r are 36,000 cm^2/Vs for electrons and 42,000 cm^2/Vs for holes and 0.83 for electrons and 1.03 for holes, respectively [31, 32]. The saturation velocity, v_{sat}, can be calculated according to an empirical formula below [29].

$$v_{\text{sat}} = \frac{v_{\text{sat}}^{300}}{\left(1 - A_v + A_v\left(\frac{T}{300}\right)\right)}. \tag{7}$$

The saturation velocity at 300 K (V_{sat}^{300}) for electrons and holes are 7×10^6 cm/s and 6.3×10^6 cm/s, respectively. The values of A_v for electrons and holes are 0.55 and 0.61, respectively [33].

Moreover, charge collection efficiency (ε_h) of a planar HPGe detector is related to λ_{trap} by [29, 30]

$$\varepsilon_h = \frac{\lambda_{\text{trap}}}{L}\left(1 - \exp\left(\frac{-L}{\lambda_{\text{trap}}}\right)\right), \tag{8}$$

where L is the detector thickness. For the known value of the net impurity concentration, and the thickness of the detector, Eq. 4 allows us to determine the charge trapping cross section (σ_{trap}) in a planar Ge detector by determining the charge collecting efficiency (ε_h).

We can determine λ_{trap} from equation 8 using the calculated values of ε_h and the known detector thickness (L). The charge carriers' combined total velocity, or (v_{tot}), is made up of their thermal velocity(v_{th}), and their saturation velocity(v_{sat}). Therefore, the electric field-dependent trapping cross section (σ_{trap}) can be calculated by combining the equations for λ_{trap} and v_{tot} [29, 34] described above.

When operating a p-type detector (RL detector) in both Mode 1 and Mode 2, the emission rate (e_n) of charge carriers from the traps can be measured. To calculate the emission rate, a specific bias voltage is applied to the detector, and the slope of the energy versus time plot is used. By combining the measured value of (e_n) with Eq. 3, we can determine the binding energies of dipole states and cluster dipole states in the p-type Ge detector at cryogenic temperatures.

4 Results and Discussion

Figures 2 and 3 display the energy deposition from ~ 5.5 MeV α particles in Mode 1 and Mode 2 of the RL detector, respectively. To determine the charge-collection efficiency of the detector, we compared the mean total energy deposited at 5.2 K with a certain bias voltage to the mean energy deposited at 77 K when the detector was depleted and operated with a bias voltage of -1200 V. For example, the mean energy observed at 77 K with a bias voltage of -1200 V was 3.92 MeV, whereas the mean energy observed at -200 V at 5.2 K was 2.09 MeV, resulting in a charge collection efficiency of 53.3% ($\varepsilon = 2.09$ MeV/3.92 MeV). We plotted the charge-collection efficiency as a function of the applied bias voltage in Fig. 4.

Using the thickness (L) of the detector (10.7 mm) and the charge-collection efficiencies obtained at various bias voltages, we calculated the trapping length (λ_{trap}) of the charge carriers with Eq. 4. Figure 5 shows the charge collection efficiency versus the trapping length.

We measured the net impurity concentration of the detector to be $6.2 \times 10^9/\text{cm}^3$ and operated it at a temperature of 5.2 K using the two modes described earlier. These values, along with other parameters presented in Eqs. 5, 7, and 8, were used to calculate the trapping cross section of the trap centers. The relationship between the trapping cross section and the applied electric field is illustrated in Fig. 6. It is worth noting that these trapping cross sections should be considered as effective trapping cross sections, as there is no known way to separate the various processes of trapping. When comparing the effective trapping cross section of the trap centers

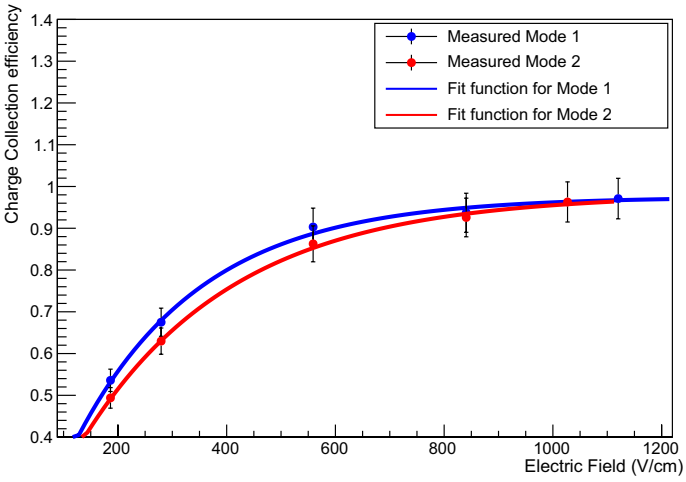

Fig. 4 The graph of charge collection efficiency (ε) versus applied electric field (E) for detector RL has been plotted, with errors taken into account. The error in ε is based on the measurement of the mean energy deposition, while the error in E is largely influenced by the bias voltage applied. A fitting model, $\varepsilon = p_0 + [(p_1 \times exp(-p_2 \times E)]$, was utilized to curve-fit the data, resulting in the following fitted parameters: For Mode 1: $p_0 = 0.974 \pm 0.044$, $p_1 = -0.994 \pm 0.0237$, and $p_2 = -0.00433 \pm 0.000145$. Similarly, for Mode 2:$p_0 = 0.9815 \pm 0.0586, p_1 = -0.9553 \pm 0.0164$,and $p_2 = -0.0035 \pm 0.00023$

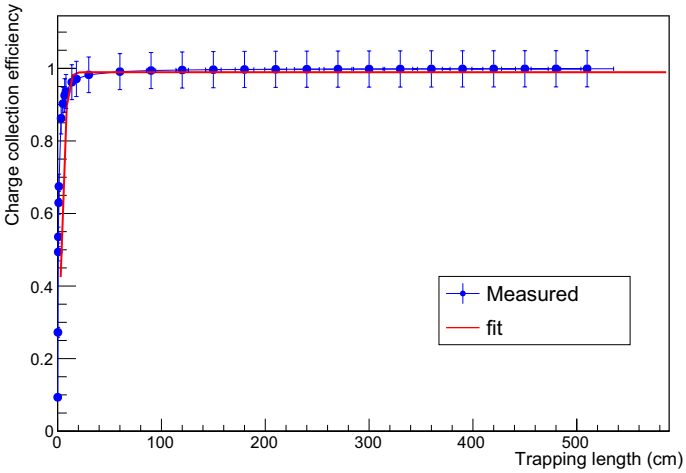

Fig. 5 The charge collection efficiency (ε) of a p-type detector RL as a function of trapping length (λ_{trap}) has been plotted, taking into account the associated errors. The error in ε is determined from the measured mean energy deposition, while the error in λ_{trap} is obtained through the propagation of error in the expression for λ_{trap} given by 8. A fitting model of the form $\varepsilon = \frac{p_0}{1+p_1 \exp(-p_2 \lambda_{\text{trap}})}$ has been applied to the data, resulting in the following fitted parameters for the p-type detector RL: $p_0 = 0.9893 \pm 0.049$, $p_1 = 4.764 \pm 0.238$, and $p_2 = 0.4335 \pm 0.0216$. This model provides a good fit to the experimental data and can be used to predict the charge collection efficiency for different values of λ_{trap}

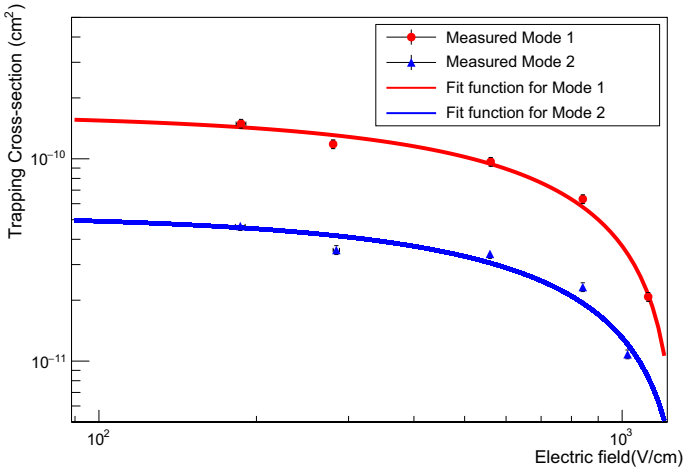

Fig. 6 The graph illustrates the relationship between the trapping cross section (σ_{trap}) and the applied bias field (E) for detector RL in both Mode 1 and Mode 2, accounting for errors. The error in σ_{trap} is determined using the propagation of error in Eq. 4, while the error in E primarily stems from the applied bias voltage. A fitting model of the form $\sigma_{\text{trap}} = p0 - [(p1) \times \exp(p2 \times E)]$ was used to fit the data. For Mode 1, the following fitted parameters were obtained: $p0 = -1.038 \times 10^{-8} \pm 3.344 \times 10^{-10}$, $p1 = -1.055 \times 10^{-8} \pm 4.336 \times 10^{-10}$, and $p2 = 1.245 \times 10^{-5} \pm 3.937 \times 10^{-7}$. Similarly, for Mode 2, the fitted parameters were found to be $p0 = -8.596 \times 10^{-10} \pm 1.24 \times 10^{-11}$, $p1 = -9.124 \times 10^{-10} \pm 8.645 \times 10^{-12}$, and $p2 = 4.527 \times 10^{-5} \pm 1.726 \times 10^{-7}$

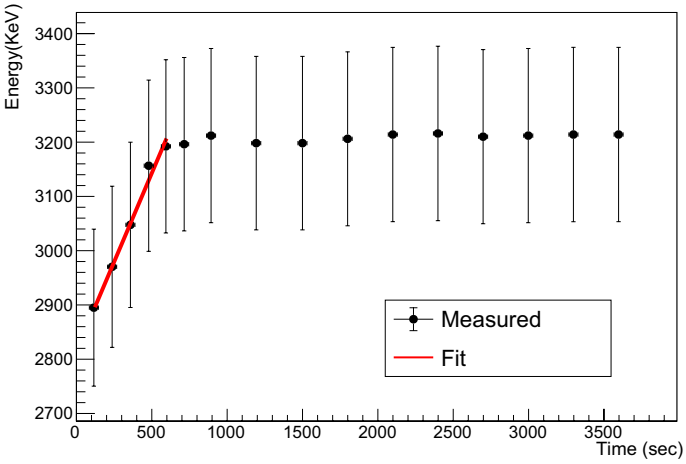

Fig. 7 The plot depicts the mean energy deposition (E_{dep}) as a function of time (t) for detector RL in Mode 2. As an illustration, the mean energy deposition (E_{dep}) and time (t) recorded for a bias voltage of 900 volts are plotted for detector RL when operated in Mode 2. The error in E_{dep} is attributed to the energy deposition determination using a Gaussian fit, while the error in t is primarily due to the recorded time determination. A linear fit ($E_{\text{dep}} = p_0 \times t + p_1$) was applied to the part of the plot where the emission of charge carriers is greater than the trapping of charge carriers. The slope (p_0) of the fit was determined to be 654.17 ± 2.76 (eV/s), and the intercept (p_1) was found to be 2821.45 ± 10.38. It should be noted that the slope represents the emission rate of charge carriers (e_n) in Eq. 3

to the charge states in Abakumov et al. [35], we found that the results are in the same order of magnitude.

We conducted a measurement of energy deposition from α-particles at 5.2 K over a period of 60 min for a given bias voltage to determine the charge emission rate mentioned in Eq. 3. During this period, we captured the histogram of energy deposition every 2–3 min, and the mean energy deposition was obtained from the α-peak. Figure 7 shows an example of this measurement for a bias voltage of 900 volts.

As depicted in Fig. 7, the application of bias voltage to the detector leads to a linear increase in the charge emission rate for the initial few minutes. This is because, in the initial minutes, de-trapping through impact ionization of dipole states or cluster dipole states outpaces the trapping of charge carriers at a given voltage. However, once the trapping and de-trapping reach a dynamic equilibrium, the energy deposition becomes constant. The slope of the plot's section, where the emission of charge carriers dominates, gives the charge-energy emission rate per unit of time, represented as e_n in Eq. 3. To convert the emission rate (e_n) into number of charge carriers, we divide e_n by the binding energy of dipole states or cluster dipole states (E_b). These emission rates in terms of the number of charge carriers per second are then used in Eq. 3 to determine the binding energy for respective dipole states or cluster dipole states. The calculated binding energies are presented in Table 1.

The binding energy of cluster dipole states is measured by the detector in Mode 2, while the binding energy of dipole states is measured by the detector in Mode 1. To measure the binding energy of cluster dipole states, we operate the detector in Mode 2, whereas for the binding energy of dipole states, we operate in Mode

Table 1 The binding energy and trapping cross section of RL at 5.2 K for Mode 1 and Mode 2

Bias voltage (V)	Electric field (V/cm)	Mode 1			Mode 2		
		Slope (eV/s)	Binding Energy (meV)	Trapping cross section (cm^2)	Slope(eV/s)	Binding Energy (meV)	Trapping cross section (cm^2)
− 200	186.92 ± 4.02	116 ± 5.80	8.105 ± 0.405	$(1.492 \pm 0.074) \times 10^{-10}$	1160 ± 58	5.807 ± 0.290	$(4.62 \pm 0.231) \times 10^{-11}$
− 300	280.37 ± 4.01	89 ± 4.45	7.916 ± 0.395	$(1.18 \pm 0.059) \times 10^{-10}$	1350 ± 67.5	5.658 ± 0.283	$(3.59 \pm 0.179) \times 10^{-11}$
− 600	560.74 ± 3.98	119 ± 5.95	7.239 ± 0.362	$(9.67 \pm 0.484) \times 10^{-11}$	1820 ± 91	5.429 ± 0.271	$(3.37 \pm 0.168) \times 10^{-11}$
− 900	841.12 ± 4.03	164 ± 8.2	6.898 ± 0.345	$(6.32 \pm 0.316) \times 10^{-11}$	654 ± 32.7	5.30 ± 0.265	$(2.32 \pm 0.116) \times 10^{-11}$
− 1100	1028.04 ± 4.01	–	–	–	871±43.55	5.237 ± 0.262	$(1.08 \pm 0.054) \times 10^{-11}$
− 1200	1121.50 ± 4.03	271 ± 13.55	6.553 ± 0.328	$(2.08 \pm 0.104) \times 10^{-11}$	–	–	–

The errors, associated with each value, are either the result of measurement errors or the error calculated from the equations used in the paper. Note that we could not get the data at − 1200 V for Mode 2 due to higher leakage current

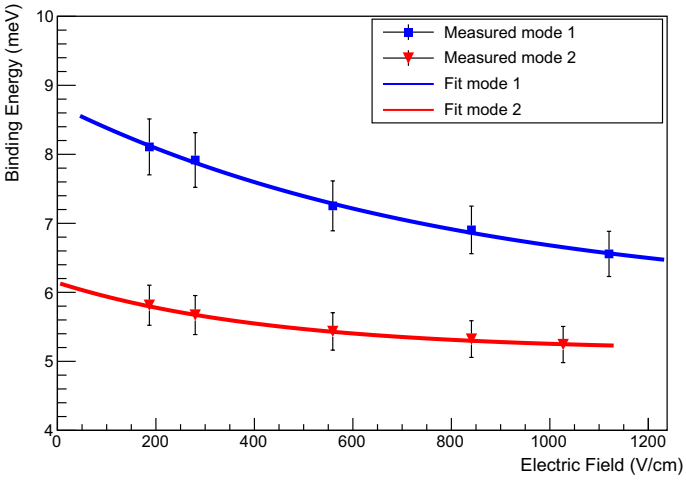

Fig. 8 The binding energies of the dipole states and the cluster dipole states have been determined as a function of the applied electric field under two different operational modes, Mode 1 and Mode 2. The error in the binding energy measurement was calculated, while the error in the electric field measurement was dominated by the precision of the applied bias voltage. To analyze the data, a fit model was used, specifically, $E_{\text{bind}} = (p_0) + (p_1) \times exp{-}(p_2) \times (E)$, which resulted in the following fitted parameters: For Mode 1, p_0 was found to be 5.845 ± 0.254, p_1 was 2.871 ± 0.184, and p_2 was 0.00123 ± 0.00003. For Mode 2, p_0, p_1, and p_2 were 5.154 ± 0.802, 0.985 ± 0.063, and 0.00229 ± 0.000068 , respectively

1. Furthermore, the binding energy values obtained at different bias voltages demonstrate a correlation with the electric field. We have depicted this relationship in Fig. 8, where the binding energies are plotted as a function of the electric field at a temperature of 5.2 K.

The dipole states (A^{0^*}) in Mode 1 exhibit binding energies ranging from 6.553 to 8.105 meV, depending on the electric field. The average binding energy, computed as the sum of $p0$ and $p1$, is 8.716 ± 0.435 meV when the electric field is zero. In contrast, the cluster dipole states (A^{+^*}) in Mode 2 have binding energies that range from 5.237 to 5.807 meV, depending on the applied electric field. The average binding energy at zero field is 6.138 ± 0.308 meV. Interestingly, the A^{0^*} states have higher binding energy at zero fields than the A^{+^*} states. Notably, both A^{0^*} and A^{+^*} states exhibit lower binding energies at zero field compared to the ground state impurity atoms in a Ge detector, which typically range in the order of 10 meV.

The populated dipole states and cluster dipole states with lower binding energies can be utilized to design a dark matter experiment with an extremely low-energy threshold, triggered by the small energy deposition through low-mass dark matter particles interacting with Ge atoms. This small energy deposition is dissipated through the emission of phonons that propagate through the detector volume and interact with dipole states or cluster dipole states, generating electron–hole pairs that are drifted toward electrodes. Our previous publication [36] demonstrates that if the detector's internal charge amplification of a factor of 100–1000 can be achieved, then the signal can be observed. It is important to note that these dipole states and cluster dipole states, which have lower binding energies, may also contribute to

device noise, depending on the detector's operating temperature environment. At extremely low temperatures, such as 5.2 K, the probability of thermal excitation from these dipole states and cluster dipole states is very low due to the small thermal energy (0.45 meV) compared to the binding energies of these states (6–8 meV). Furthermore, the device noise is distributed across a broader range of energies, and their nature can be discerned and separated using techniques like low-pass or high-pass filters during calibration. By exciting the dipole and cluster dipole states, low-mass dark matter-induced events with lower energies can be statistically identified, depending on the event rate.

5 Conclusion

Our investigation of binding energies and trapping cross sections in a p-type Ge detector at low temperatures has yielded important insights. Our measurements show that the binding energy of dipole states is 8.716 ± 0.435 meV, while the binding energy of cluster dipoles is 6.138 ± 0.308 meV, which is lower than the typical binding energy of ground state impurities in Ge. These binding energies are thermally stable at 5.2 K, and applying an electric field causes increased de-trapping via impact ionization for cluster dipoles due to their smaller binding energy compared to dipole states.

The trapping cross section, ranging from 1.08×10^{-11} cm^2 to 1.492×10^{-10} cm^2, is primarily influenced by the electric field, with increasing electric fields leading to decreased binding energies and trapping cross sections. These low binding energies suggest the possibility of developing a low-threshold detector for low-mass dark matter searches using appropriately doped impurities in Ge.

Overall, our findings provide valuable insights into the behavior of impurities in Ge detectors, which could inform the development of new detectors for dark matter searches and other applications.

Acknowledgements The authors are grateful to Mark Amman for providing instructions on how to construct planar detectors. We also acknowledge the contribution of a test cryostat from the Nuclear Science Division of the Lawrence Berkeley National Laboratory. This research was funded in part by NSF OISE 1743790, DE-SC0004768, and a South Dakota governor's research center.

Author Contributions Mr. Mathbar Raut played an integral role in conducting measurements, performing data analysis, and drafting the initial version of the paper. Prof. Dongming Mei, who led the project, was instrumental in developing experimental ideas and provided crucial supervision during the data collection and analysis phases. His vast experience in the field was invaluable in ensuring the accuracy and quality of our research. Additionally, he revised the manuscript, making it comprehensive and concise. Mr. Sanjay Bhattarai was also a key member of the team, participating in the data analysis and providing valuable insights that helped refine our findings. Dr. Rajendra Panth, who fabricated the detector and created the analysis framework, played a critical role in ensuring the validity and reliability of our results. Mr. Kyler Kooi established the pulse tube refrigerator and ensured the proper functioning of the data acquisition system. Dr. Hao Mei and Dr. Guojian Wang provided the high-quality detector-grade crystals that were grown at USD.

Funding Department of Energy of the United States, DE-SC0004768 and National Science Foundation of the United States, NSF OISE 17437980.

Availability of Data and Materials The data used for the analysis are included in the manuscript.

Declarations

Conflict of interest The authors declare no competing interests.

Ethical Approval Not applicable.

References

1. M. Lazarević, Stability and stabilization of fractional order time delay systems. Sci. Tech. Rev. **61**, 31–45 (2011)
2. E. Armengaud et al., Searches for electron interactions induced by new physics in the edelweiss-iii germanium bolometers. Phys. Rev. D **98**, 082004 (2018)
3. W. Zhao et al., (CDEX Collaboration), First results on low-mass wimps from the cdex-1 experiment at the china jinping underground laboratory. Phys. Rev. D **88**, 052004 (2013)
4. W.Z. Wei et al., Investigation of amorphous germanium contact properties with planar detectors made from usd-grown germanium crystals. J. Instrum. **13**, P12026 (2018)
5. R. Essig, J. Mardon, T. Volansky, Direct detection of sub-gev dark matter. Phys. Rev. D **85**, 076007 (2012)
6. G. Adhikari et al., (COSINE-100 Collaboration), Searching for low-mass dark matter via the migdal effect in cosine-100. Phys. Rev. D **105**, 042006 (2022)
7. F. Petricca et al., First results on low-mass dark matter from the cresst-iii experiment. J. Phys. Conf. Ser. **1342**, 012076 (2020)
8. K.M. Sundqvist et al., A measurement of electron and hole drift velocities in a germanium< 100> cdms detector, at a temperature of 31 millikelvin, in AIP Conference Proceedings, Vol. 1185 (American Institute of Physics, 2009) pp. 128–131
9. R. Agnese et al., Search for low-mass dark matter with cdmslite using a profile likelihood fit. Phys. Rev. D **99**, 062001 (2019)
10. J.-P. Richard, Time-delay systems: an overview of some recent advances and open problems. Automatica **39**, 1667–1694 (2003)
11. N. Severijns, B. Blank, Weak interaction physics at isolde. J. Phys. G Nucl. Part. Phys. **44**, 074002 (2017)
12. W.-Z. Wei, D.-M. Mei, Average energy expended per eh pair for germanium-based dark matter experiments. J. Instrum. **12**, P04022 (2017)
13. D.M. Mei et al., Evidence of cluster dipole states in germanium detectors operating at temperatures below 10 k. AIP Adv. **12**, 065113 (2022)
14. S. Bhattarai, D. Mei, M. Raut, Low-energy solar neutrino detection utilizing advanced germanium detectors. J. Phys. G Nucl. Part. Phys. (2023). https://doi.org/10.1088/1361-6471/acc751
15. N.S. Zákoucký, B. Vereecke, S. Versyck, Hpge detectors for low-temperature nuclear orientation. Nucl. Instrum. Methods Phys. Res. Sect. A Accel. Spectrom. Detect. Assoc. Equip. **520**, 80–83 (2004)
16. A. Nagih, G. Plateau, Fractional problems: overview of applications and solutions. Rairo-Recherche Operationnelle-Operations Research **33**, 383–419 (1999)
17. J.F. Ziegler, M.D. Ziegler, J.P. Biersack, Srim-the stopping and range of ions in matter. Nucl. Instrum. Methods Phys. Res. Sect. B **268**, 1818–1823 (2010)
18. I.J. Arnquist et al., α-event characterization and rejection in point-contact hpge detectors. Eur. Phys. J. C **82**, 226 (2022)
19. J. Leon et al., Noise considerations for a very low threshold semiconductor detector system, in 2012 IEEE Nuclear Science Symposium and Medical Imaging Conference Record (NSS/MIC) (2012) pp. 868–871
20. S. Bhattarai et al., Development of low-threshold detectors for low-mass dark matter searches using an n-type germanium detector at 5.2 k, arXiv preprint arXiv:2302.08414 (2023)
21. M.S. Raut et al., Characterization of high-purity germanium (ge) crystals for developing novel ge detectors. J. Instrum. **15**, T10010 (2020)

22. G. Yang et al., Investigation of influential factors on the purification of zone-refined germanium ingot. Cryst. Res. Technol. **49**, 269–275 (2014)
23. G. Wang et al., Development of large size high-purity germanium crystal growth. J. Cryst. Growth **352**, 27–30 (2012)
24. S. Bhattarai et al., Investigation of the electrical conduction mechanisms in p-type amorphous germanium electrical contacts for germanium detectors in searching for rare-event physics. Eur. Phys. J. C **80**, 1–10 (2020)
25. X.H. Meng et al., Fabrication and characterization high-purity germanium detectors with amorphous germanium contacts. J. Instrum. **14**, P02019 (2019)
26. R. Panth et al., Implication of the temperature-dependent charge barrier height of amorphous germanium contact detector in searching for rare event physics, arXiv e-prints, arXiv–2101 (2021)
27. E.Y. Lee et al., Compensation and trapping in cdznte radiation detectors studied by thermoelectric emission spectroscopy, thermally stimulated conductivity, and current-voltage measurements. J. Electron. Mater. **28**, 766–773 (1999)
28. R. Agnese et al., Search for low-mass weakly interacting massive particles with supercdms. Phys. Rev. Lett. **112**, 241302 (2014)
29. D.M. Mei et al., Impact of charge trapping on the energy resolution of ge detectors for rare-event physics searches. J. Phys. G Nucl. Part. Phys. **47**, 105106 (2020)
30. Z. He, Review of the Shockley–Ramo theorem and its application in semiconductor gamma-ray detectors. Nucl. Instrum. Methods Phys. Res. Sect. A **463**, 250–267 (2001)
31. R. Quay et al., A temperature dependent model for the saturation velocity in semiconductor materials. Mater. Sci. Semicond. Process. **3**, 149–155 (2000)
32. N. Abrosimov et al., Technology development of high purity germanium crystals for radiation detectors. J. Cryst. Growth **532**, 125396 (2020)
33. Z. Ahmed et al., Results from a low-energy analysis of the CDMS II germanium data. Phys. Rev. Lett. **106** (2011)
34. A.T.J. Phipps, Ionization Collection in Detectors of the Cryogenic Dark Matter Search, Ph.D. thesis, school University of California, Berkeley (2016)
35. V.N. Abakumov et al., Nonradiative recombination in semiconductors. Mod. Probl. Condens Matter Sci. **33**, 50 (1991)
36. D.-M. Mei et al., Direct detection of mev-scale dark matter utilizing germanium internal amplification for the charge created by the ionization of impurities. Eur. Phys. J. C **78**, 187 (2018)